Springer Oceanography

Manuel G. Velarde
Roman Yu. Tarakanov
Alexey V. Marchenko *Editors*

The Ocean in Motion

Circulation, Waves, Polar Oceanography

Springer

Abyssal Mixing in the Laboratory

T. Dauxois, E. Ermanyuk, C. Brouzet, S. Joubaud and I. Sibgatullin

Motivation

The continuous energy input to the ocean interior comes from the interaction of global tides with the bottom topography yielding a global rate of energy conversion to internal tides of the order of 1TW [1, 2]. The subsequent mechanical energy cascade to small-scale internal-wave motion and mixing is a subject of active debate in view of the important role played by abyssal mixing in existing models of ocean dynamics. The oceanographic data support the important role of internal waves in mixing, at least locally: increased rates of diapycnal mixing are reported [3] in the bulk of abyssal regions over rough topography in contrast to regions with smooth bottom topography. A question remains: how does energy injected through internal waves at large vertical scales induce the mixing of the fluid?

Using laboratory experiments and numerical simulations, we suggest the energy cascade in internal wave attractors as a novel laboratory model of a natural cascade. We show that energy transfer from global to small scales in attractors operates via a hierarchy of triadic resonant interactions producing a complex internal wave

T. Dauxois (✉) · C. Brouzet · S. Joubaud
Univ Lyon, ENS de Lyon, Univ Claude Bernard Lyon 1, CNRS,
Laboratoire de Physique, 69342 Lyon, France
e-mail: thierry.dauxois@ens-lyon.fr

C. Brouzet
e-mail: Christophe.brouzet@ens-lyon.fr

S. Joubaud
e-mail: Sylvain.Joubaud@ens-lyon.fr

E. Ermanyuk
Lavrentyev Institute of Hydrodynamics, Novosibirsk, Russia
e-mail: ermanyuk@hydro.nsc.ru

I. Sibgatullin
Faculty of Mechanics and Mathematics, Moscow State University, Moscow, Russia
e-mail: sibgat@ocean.ru

I. Sibgatullin
Shirshov Institute of Oceanology, Russian Academy of Sciences, Moscow, Russia

M. G. Velarde et al. (eds.), *The Ocean in Motion*, Springer Oceanography,
https://doi.org/10.1007/978-3-319-71934-4_16

field with a rich multi-peak discrete frequency spectrum embedded into a continuous spectrum of weaker magnitude. Convincing evidences of a wave turbulence framework [4] for internal waves are also provided. Spontaneous summation of the wave-field components produces moreover a statistically significant amount of extreme overturning events which eventually lead to a well-measurable mixing. This suggests that such a set-up is appropriate to study abyssal mixing in the laboratory.

Let us consider a stratified fluid with an initially constant buoyancy frequency $N = [(-g/\bar{\rho})(\mathrm{d}\rho/\mathrm{d}z)]^{1/2}$, where $\rho(z)$ is the density distribution over the vertical coordinate z, $\bar{\rho}$, and g the gravity acceleration. The dispersion relation for linear internal gravity waves is given by

$$\theta = \pm \arcsin \Omega, \tag{1}$$

where θ is the slope of the wave beam to the horizontal, and Ω (resp. $\omega = \Omega N$) the non-dimensional (resp. dimensional) frequency of oscillations. This anisotropic dispersion relation requires preservation of the slope of the internal wave beam upon reflection at a rigid boundary. As we will recall below, in the case of a sloping boundary, this property gives a purely geometric reason for a strong variation of the width of internal wave beams (focusing or defocusing) upon reflection. Internal wave focusing provides a necessary condition for large shear and overturning, as well as shear and bottom layer instabilities at slopes.

In a confined fluid domain, focusing usually prevails, leading to a concentration of wave energy on a closed loop, the internal wave attractor [5]. At the level of linear mechanisms, the width of the attractor branches is set by the competition between geometric focusing and viscous broadening. (see [6] for a precise and interesting of this question). High concentration of energy at attractors make them prone to triadic resonance instability which sets in as the energy injected into the system increases [7]. Note that the particular case for which both secondary waves have a frequency equal to half of the forcing frequency is of special interest in the oceanographic context where viscosity is negligible. In that case, the appropriate name is parametric subharmonic instability and abbreviated as PSI. By abuse of language, some authors have sometimes extended the use of the name PSI to cases for which secondary waves are not corresponding to half of the forcing frequency. For the sake of terminological consistency, we propose to abbreviate triadic resonance instability using the acronym TRI.

The onset of instability is similar to the classic concept of triadic resonance, which is best studied for the idealized case, with monochromatic in time and space carrier wave as a basic state which feeds two secondary waves via nonlinear resonant interactions. The resonance occurs when temporal $\Omega_1 + \Omega_2 = \Omega_0$ and spatial $\mathbf{k_1} + \mathbf{k_2} = \mathbf{k_0}$ conditions are satisfied ($\mathbf{k}$ is the wave vector while subscripts 0, 1 and 2 refer to the primary, and two secondary waves, respectively). In a wave attractor, the wave beams serve as a primary wave, and the resonance conditions are satisfied with a good accuracy [7], providing a consistent physical framework for the short-term behavior of the instability.

The usual theory for the TRI does not take into account the finite width of the experimental beam. Qualitatively, the subharmonic waves can serve as an energy

sink for the primary wave if they do not leave the primary beam before they can extract substantial energy [8]. The group velocity of the primary wave is aligned with the beam, but the group velocity of the secondary waves is definitely not, and these secondary waves eventually leave the primary wave beam. This is a direct consequence of the dispersion relation (1), which relates the direction of propagation to the frequency: a different frequency, smaller for subharmonic waves, will lead to a shallower angle. The generalization to wave beams with a finite width is presented in detail in a recent review [9].

The Internal Wave Attractor to Enhance the Nonlinearities

In this section, we present the concept of internal wave attractor that is a key element to provide large amplitude internal wave beams produced thanks to the focusing properties of internal wave reflections.

Reflection of Internal Waves: A Focusing Mechanism

The dispersion relation of internal waves is very specific and leads to a very unusual reflection on a sloping boundary that has interesting properties, central for our objective as it will be immediately clear. To be more specific, let us consider an inviscid linearly stratified fluid of constant buoyancy frequency N and a sloping boundary, tilted with an angle α with respect to the vertical, as shown in Fig. 1. Note that, if this configuration does not seem natural for the reflection of internal waves on the topography at the bottom of the ocean, it corresponds by symmetry to a case with negative values of α, but is simpler for an experimental realization.

As the pulsation of the wave is conserved during the reflection, both the incident and reflected waves propagate with the same angle θ, according to the dispersion relation (1). It is worth to note that this is very different from the reflection in optics or acoustics where the electromagnetic or sound waves conserve the angle with respect to the normal to the sloping boundary, refereed usually as the classical Descartes reflection. For internal waves, this is the angle with the gravity that is conserved. This difference is illustrated in Fig. 1a. The reflected ray for optics or acoustics is the dashed arrow while the one for internal waves is the solid arrow.

This non-Descartes reflection is even more intriguing, and therefore interesting, when one considers a beam, and not only a ray. This is shown in Fig. 1b. The width of the reflected beam is thus reduced and one gets an energy focusing for these internal waves. It is important to emphasize that this phenomenon being a direct consequence of the linear dispersion relation, one has identified here a linear transfer toward smaller scales.

Note that for the two specific cases of a wall being vertical or horizontal ($\alpha = 0$ or $\pi/2$), the reflection of an internal wave is similar to a classical Descartes reflection, without any focusing effect.

The Focusing Parameter

It is of course possible to get more quantitative results. The linear theory of internal wave reflection has been developed first by Phillips [10] and is based on a well-known incident wave reflecting at a sloping boundary. Let assume that the incident wave is bi-dimensional (in the vertical plane) and can be described by the stream function

$$\psi_{\mathrm{i}}(x,z,t) = \psi_{0,\mathrm{i}} \exp\left[i\left(\omega_{\mathrm{i}}\, t - \mathbf{k}_{\mathrm{i}} \cdot \mathbf{r}\right)\right]. \tag{2}$$

The index i refers to the incident wave field, while ω_{i} and $\mathbf{k}_{\mathrm{i}}$ are the pulsation and wave vector of the incident wave and satisfy the dispersion relation (1). With u and w the horizontal and vertical velocity fields, the kinetic energy density is defined as

$$E_{c,\mathrm{i}} = \frac{1}{2}\bar{\rho}\left(|u|^2 + |w|^2\right) = \frac{1}{2}\bar{\rho}\left(|\partial_z \psi_{\mathrm{i}}|^2 + |\partial_x \psi_{\mathrm{i}}|^2\right) = \frac{1}{2}\bar{\rho} k_{\mathrm{i}}^2 |\psi_{0,\mathrm{i}}|^2. \tag{3}$$

When the incident wave hits the sloping boundary, a reflected wave is generated and can be expressed as follows

$$\psi_{\mathrm{r}}(x,z,t) = \psi_{0,\mathrm{r}} \exp\left[i\left(\omega_{\mathrm{r}}\, t - \mathbf{k}_{\mathrm{r}} \cdot \mathbf{r}\right)\right], \tag{4}$$

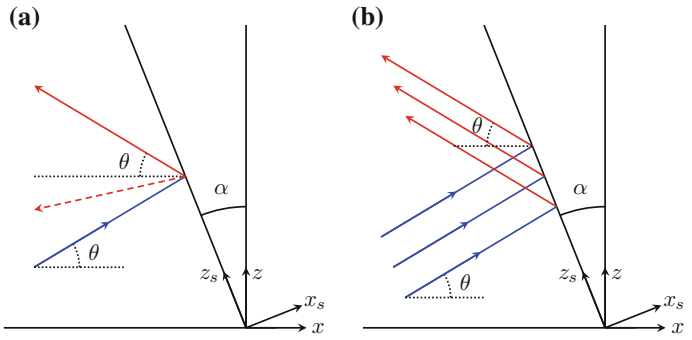

Fig. 1 **a** Reflection of an incident ray on the sloping boundary inclined with an angle α with respect to the vertical. In optics or acoustics, the reflected ray is along the dashed arrow, while for internal waves, the reflected ray is along the solid arrow. **b** Reflection of an incident internal wave beam on a sloping boundary for internal waves. The slope coordinates (x_s, z_s) are shown on both panels

where the index r refers to the reflected wave field. Its kinetic energy density corresponds to $E_{c,\mathrm{r}} = \frac{1}{2}\bar{\rho}k_{\mathrm{r}}^2|\psi_{0,\mathrm{r}}|^2$. The complete wave field is therefore $\psi = \psi_{\mathrm{i}} + \psi_{\mathrm{r}}$.

As the flow does not penetrate the sloping boundary, the total stream function field must vanish at the boundary defined by $x = -z\tan\alpha$. In order to simplify the boundary condition, one usually defines the coordinates attached to the slope (x_s, z_s), as shown in Fig. 1. The velocity fields in the slope coordinate system are $(u_s, w_s) = (-\partial\psi/\partial z_s, \partial\psi/\partial x_s)$ and the wave number is noted $\mathbf{k}_s = (k_{x_s}, k_{z_s})$. The non-penetration condition can be expressed as $u_s = 0$ at $x_s = 0$ and for all z_s and time t. On the total stream function field, this becomes

$$k_{z_s,\mathrm{i}}\psi_{0,\mathrm{i}}\exp\left[i\left(\omega_{\mathrm{i}}\,t - \mathbf{k}_{s,\mathrm{i}}\cdot\mathbf{r}_s\right)\right] + k_{z_s,\mathrm{r}}\psi_{0,\mathrm{r}}\exp\left[i\left(\omega_{\mathrm{r}}\,t - \mathbf{k}_{s,\mathrm{r}}\cdot\mathbf{r}_s\right)\right] = 0, \tag{5}$$

at $x_s = 0$ and for all z_s and time t. This leads to $\omega_{\mathrm{i}} = \omega_{\mathrm{r}} \equiv \omega$, $k_{z_s,\mathrm{i}} = k_{z_s,\mathrm{r}}$ and $\psi_{0,\mathrm{i}} = \psi_{0,\mathrm{r}} \equiv \psi_0$. Thus, the frequency and the wave vector component parallel to the sloping boundary are conserved during the reflection. The normal component of the wave vector can be determined using geometrical construction and the dispersion relation: one gets $k_{x_s,\mathrm{i}} = k_{z_s,\mathrm{i}}\tan(\theta - \alpha)$ and $k_{x_s,\mathrm{r}} = k_{z_s,\mathrm{r}}\tan(\theta + \alpha)$. Thus, the ratio between the norms of the two wave vectors is given by

$$\frac{k_{\mathrm{r}}}{k_{\mathrm{i}}} = \left|\frac{\cos(\theta - \alpha)}{\cos(\theta + \alpha)}\right| \equiv \gamma. \tag{6}$$

This defines the focusing parameter γ. Equation (6) confirms immediately that there is neither focusing, nor defocusing when the wall is vertical ($\alpha = 0$) or horizontal ($\alpha = \pi/2$): both cases lead indeed to $\gamma = 1$. One recovers indeed the case of the Descartes reflection, since keeping the angle with respect to the gravity for the internal waves, does correspond to keep the angle with respect to the normal of the wall (that is orthogonal or parallel to the gravity!).

However as soon as one considers a sloping boundary ($\alpha \neq 0$) or ($\alpha \neq \pi/2$), the focusing parameter is different from unity: it is for example greater than 1 in Fig. 1. The width of the reflected beam is thus reduced by the factor γ. This is a focusing reflection, the energy in the incident beam being concentrated. Indeed, Eq. (6) leads to $E_{c,\mathrm{r}} = \gamma^2 E_{c,\mathrm{i}}$ showing that the energy density is increased by a factor $\gamma^2 > 1$.

Interestingly, this parameter diverges when $\theta + \alpha$ tends to 90°. This corresponds to the case where the waves have a propagation angle very close to the slope of the wall. This situation is called critical reflection. Indeed, it is critical because γ diverges and thus, the wave length of the reflected wave tends to 0: nonlinear and dissipation effects cannot be overlooked and should be treated carefully. Using a weakly nonlinear theory, it has been shown [11] how to heal this singularity using matched asymptotic expansion. This is however not the case under study in the remainder of this work.

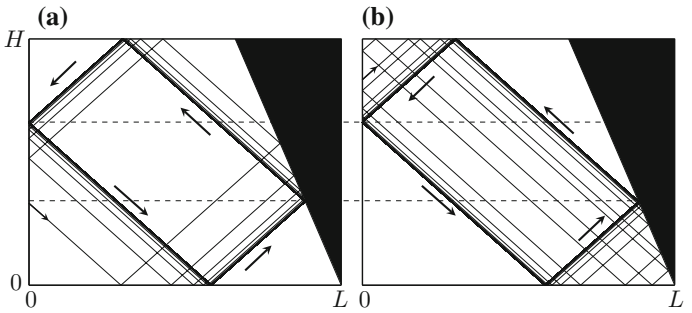

Fig. 2 Convergence towards the same attractor of two rays starting from two different points in the same geometry. The small arrows on the left vertical wall indicate the two positions where the rays start, while the large arrows show the direction of propagation of the periodic ray on the attractor. The two horizontal dashed lines show that the two attractors reached are exactly identical

An Internal Wave Billiard

If one considers now a closed basin as illustrated in Fig. 2, one realizes that the above focusing mechanism will lead to an extremely efficient focusing phenomenon. After the first reflection on the sloping wall, the beam depicted in Fig. 1b will reflect on the surface, then on the left vertical wall, and then on the bottom horizontal surface. These three Descartes-like reflections ($\alpha = 0$ or $\pi/2$) do not change neither the energy density nor the norms of the two wave vectors. However the following reflection on the sloping wall will again reduce the beam by a similar factor: it is straightforward to understand that after a few loops the beam will be extremely narrow, and indeed its width will inevitably vanish in the limit of infinitely many reflections, leading to a single ray bouncing on the walls.

Internal wave ray tracing in different closed basin shapes has been essentially studied by Leo Maas over the last twenty years. This can be viewed as an internal wave billiard [12]. The classical billiard studies the trajectories in a closed domain of a particle reflecting elastically and following the standard Descartes reflection. It can exhibit periodic motion, motion along an invariant curve or chaos [13].

In a trapezoidal domain, different attractors have been identified and carefully studied [5]. They are labelled using two indices: the number of reflections at the surface (or at the bottom) and the number of reflections on the vertical side wall (or on the slope). Figure 2 presents an attractor with only one reflection on the surface and on the vertical wall: a (1,1) attractor as the one we will use in the remainder of the paper.

However, the internal attractor is not the goal of our study, but rather the tool to drive strong instabilities within the fluid. As we have understood from the above discussion, already within the linear regime, such a wave attractor has an extremely efficient focusing power and nonlinearity will come into play, leading to triadic resonance instabilities that will drive efficiently the wave turbulence.

Experimental and Numerical Set-Up

We have combined numerical and experimental approaches to study the dynamics of stable and unstable internal wave attractors. The problem is considered in a classic trapezoidal set-up filled with a uniformly stratified fluid. Energy is injected into the system at global scale by the small-amplitude motion of a vertical wall.

Experimental Set-Up

The experimental set-up [7, 16] is sketched in Fig. 3. Experiments are conducted in a rectangular test tank of size $80 \times 17 \times 42.5$ cm^3 filled with uniformly stratified fluid using the conventional double-bucket technique. Salt is used as a stratifying agent. The density profile is measured prior and after experiments by a conductivity probe attached to a vertical traverse mechanism. The value of the buoyancy frequency N is evaluated from the measured density profile. The trapezoidal fluid domain of length L (measured along the bottom) and depth H is delimited by a sliding sloping wall, inclined at the angle α. The wall is slowly inserted into the fluid after the end of the filling procedure. The input forcing is introduced into the system by an internal wave generator [18, 19]. The time-dependent vertical profile of the generator is prescribed in the form

$$\zeta(z,t) = a \sin(\omega_0 t) \cos(\pi z/H), \tag{7}$$

where a and ω_0 are the amplitude and frequency of oscillations, respectively. In a horizontally semi-infinite domain, the motion of the generator would generate the first vertical mode of internal waves. The profile given in Eq. (7) is reproduced in discrete

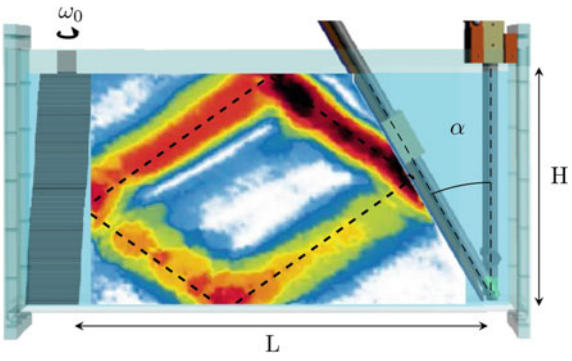

Fig. 3 The wave generator is on the left and the inclined slope on the right. A typical PIV snapshot showing the magnitude of the experimental two-dimensional velocity field obtained after 15 periods $T_0 = 2\pi/(N\Omega_0)$ of forcing is presented. Dashed lines show the billiard geometric prediction of the attractor

form by the horizontal motion of a stack of 47 plates. The whole-field velocity measurements are performed via the standard Particle Image Velocimetry (PIV) technique. To achieve this, the fluid is seeded with light-reflecting hollow glass spheres of size 8 μm and density 1100 kg/m^3. The sedimentation velocity of such particles is found to be very low, with negligible effect on results of velocity measurements. The longitudinal $(x, y = 0, z)$ mid-plane of the test section is illuminated by a vertical laser sheet coming through the side of the tank. The PIV acquisition leads to 2 velocity fields per second. This sampling rate is found to provide a sufficient resolution of the significant frequency components of the signal and the mesh of measurements is also found to be sufficient to resolve the small-scale details of the wave field.

Numerical Computations

Numerical computations were performed with a spectral element method [14, 15], using the modified open code nek5000. The geometry of the numerical set-up closely reproduces the experimental one. The full system of equations being solved consists of the Navier-Stokes equation in the Boussinesq approximation, the continuity equation and the equation for the transport of salt. Typical meshes used in calculations consist of 50 thousands to half-million elements, with 8 to 10-order polynomial decomposition within each element. Time discretization was 10^{-4} to 10^{-5} of the external forcing period. Comparisons of experimental and numerical results present a beautiful agreement, not only qualitative but also quantitative [16].

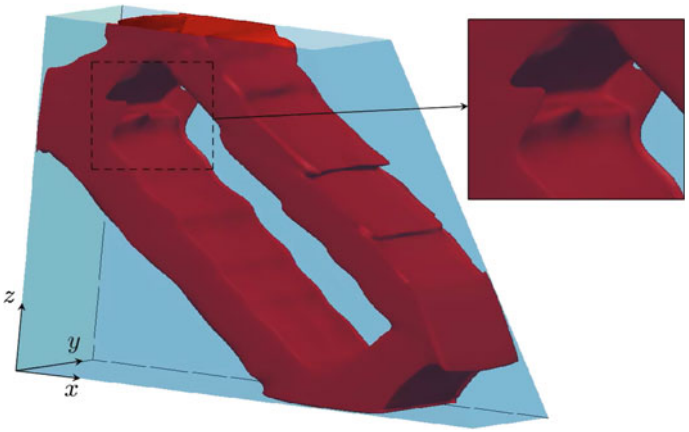

Fig. 4 Visualization of the three dimensional effects in the internal wave attractor. Snapshot of the instantaneous magnitude of the velocity field $(u^2 + w^2)^{1/2}$ produced by the 3D numerical simulations based on the spectral element method for $a = 2.4$ mm. The snapshot corresponds to a contour plot (level 0.25 cm/s) of the amplitude of the velocity field $(u^2 + w^2)^{1/2}$ at $t = 50\,T_0$. The inset presents a zoom to emphasize an example in which the flow field is dependent of the transverse direction

Figure 4 reveals the onset of TRI in the attractor. The numerical simulations clearly emphasize the importance of boundary layers close to the walls, and thus the importance of the three-dimensionality to recover experimental laboratory results quantitatively, nevertheless 2D simulations are fully sufficient for qualitative agreement. We checked [7, 16], that the temporal and spatial resonance conditions of TRI are satisfied experimentally and numerically.

Comparison

We have carefully compared the results obtained experimentally and numerically. Two examples are shown in Figs. 5 and 6, respectively for a stable and an unstable attractor. In both cases, the wave frequency is $\Omega_0 = 0.62 \pm 0.01$. Note that in the calculation, a piecewise linear approximation of the experimental density profile has been taken, with the lower layer of depth $H' = 30.8$ cm and buoyancy frequency N, and the upper layer of depth $\delta = 1.8$ cm with a density gradient 8 times smaller. The total depth of the fluid is therefore $H = H' + \delta = 32.6$ cm. The comparison emphasizes how precise are the two approaches, especially if one notes that the shade scale is the same in both panels.

More detailed comparisons can be found in [16, 17], where we showed that the results of three-dimensional calculations are in excellent qualitative and quantitative agreement with the experimental data, including the spatial and temporal parameters of the secondary waves produced by triadic resonance instability. Further, we explored experimentally and numerically the effect of lateral walls on secondary currents and spanwise distribution of velocity amplitudes in the wave beams.

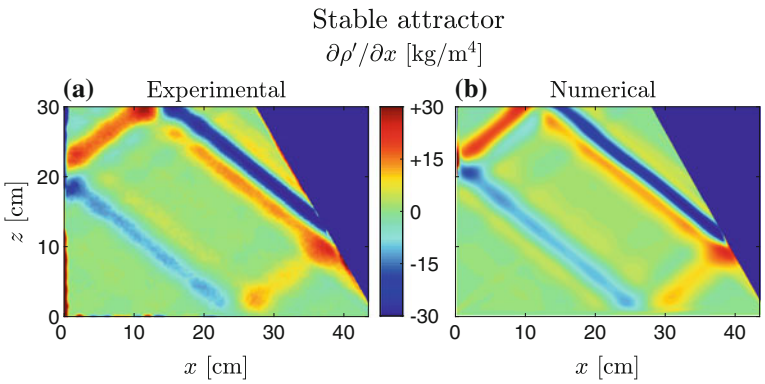

Fig. 5 Experimental (**a**) and numerical (**b**) snapshots of the horizontal density gradient at $t = 50\ T_0$ for a stable attractor. The amplitude of the wave maker is $a = 2$ mm for the experiment and $a = 1.8$ mm for the simulation

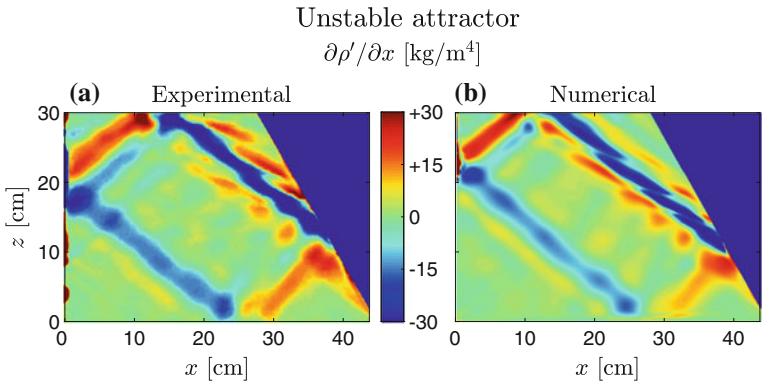

Fig. 6 Experimental (**a**) and numerical (**b**) snapshots of the horizontal density gradient at $t = 50\,T_0$ for an unstable attractor. The amplitude of the wave maker is $a = 2.5$ mm for the experiment and $a = 2.4$ mm for the numerical simulation

Finally, we tested the assumption of a bidimensional flow and estimated the error made in synthetic schlieren measurements due to this assumption.

The Energy Cascade Revealed by the Time-Frequency Diagram and the Bicoherence Plot

Using laboratory experiments and numerical simulations, we have shown that the internal wave attractor set-up, sketched in Fig. 3, provides an excellent energy cascade, emphasizing how internal wave attractors can be a novel laboratory model of a natural cascade [20].

Indeed, the internal wave attractor is the first step: the focalisation mechanism enhances the development of the triadic instability within the beams of the attractor. While the attractor is still visible, branches are progressively deformed by triadic resonance instability, leading to the presence of secondary waves.

An example of an experimental velocity field is shown in Fig. 7 at a late stage. The attractor is still visible, but branches are deformed by the presence of secondary waves. As it will be clear below, the internal wave frequency spectrum which was initially a Dirac function has been progressively enriched to give rise to a very complex spectrum, through a cascade of central interest.

Once the instability is well-developed, secondary waves are acting as primary waves for higher-order triadic interactions. If the focalisation is strong enough, this mechanism will of course repeat through the instability of the secondary waves. This is what is revealed by the time frequency diagram shown in Fig. 8a. Initially, only a signal around $\Omega_0 = 0.61$ is present, but almost immediately one distinguishes two secondary waves $\Omega_1 = 0.36$ and $\Omega_2 = 0.25$ whose sum gives Ω_0. However, again Ω_1 and Ω_2 are destabilized and this mechanism is pursued.

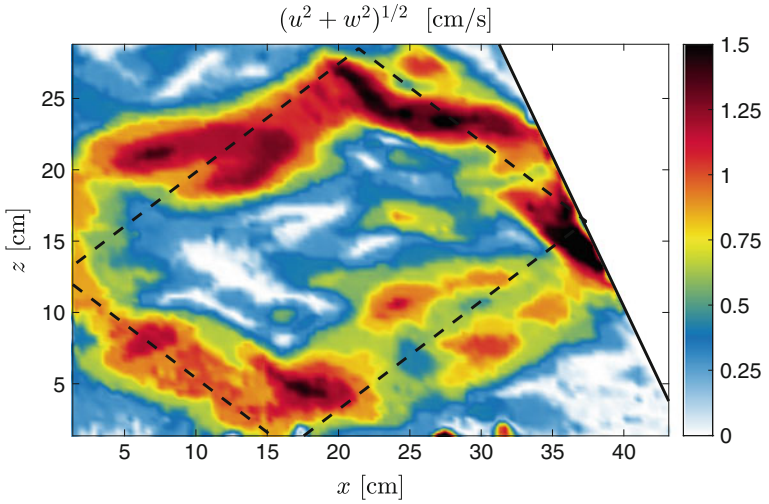

Fig. 7 Magnitude of the experimental two-dimensional velocity field at $t = 400\,T_0$ for $a = 5$ mm. Dashed lines show the billiard geometric prediction of the attractor, which is fully recovered when considering small forcing amplitude or at an earlier time when considering larger forcing

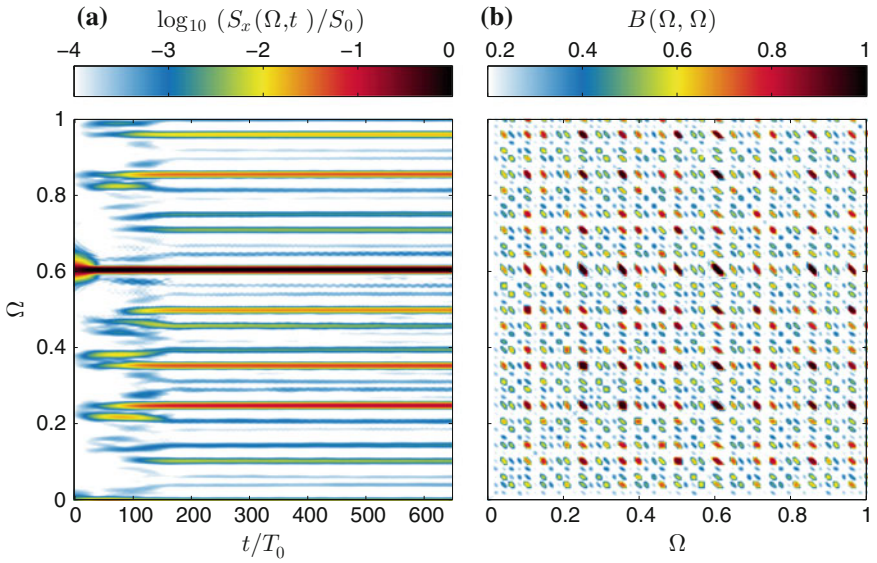

Fig. 8 Time-frequency diagram (**a**) and its associated bicoherence (**b**) of the PIV signal measured in a 5×5 cm^2 square centered around the most energetic branch of the attractor, after the focusing reflection

To detect the frequency triplets, we use the bispectrum analysis which measures the extent of statistical dependence among three spectral components (Ω_k, Ω_i, Ω_j) satisfying the relationship $\Omega_k = \Omega_i + \Omega_j$, with the quantity $M(\Omega_i, \Omega_j) = F(\Omega_i)F(\Omega_j)F^*(\Omega_i + \Omega_j)$, where F is the Fourier transform and $*$ denotes the complex conjugate. In practice, the bispectrum is usually normalized and considered in form of bicoherence which is 0 for triplets with random phases and 1 for triplets with perfect phase coupling. The bicoherence is shown in Fig. 8b. In addition to the strong peak $(0.61, 0.61)$ corresponding to the forcing frequency (therefore to self-correlation), the possible triplets satisfying the definition of triadic resonance at $\Omega_k = \Omega_0$ can be found on the line with slope -1 connecting the points $(0, 0.61)$ and $(0.61, 0)$. This emphasizes that the mechanism at play is triadic. Other peaks are also visible corresponding to other choices of Ω_k revealing that the instability mechanism is repeated and leads to a cascade.

Thanks to this beautiful representation, it can therefore be attested that the energy transfer from global to small scales in attractors operates via a hierarchy of triadic interactions producing a complex internal wave field with a rich multi-peak discrete frequency spectrum embedded in a continuous spectrum of weaker magnitude.

The bicoherence demonstration of the cascade is closely related to the bispectrum shown in Fig. 8b. Both axis represent frequencies, and the color on the bispectrum diagram is proportional to the product of the amplitudes. From this picture it can be also be easily seen that the amplitude of the daughter waves tend to lie on the antidiagonals. On very long time intervals the picture shown in Fig. 8b can be changed significantly due to slow evolution of the nonlinear interactions to a completely new regime.

A Route Towards Wave Turbulence

It is important to emphasize that the final stage is non-trivial since these phenomena are beyond the domain of pure wave-wave interactions: it corresponds to a regime usually called wave turbulence [4]. A similar situation takes place for surface waves, where the flourishing literature gives a fully consistent description of energy cascades between components of wave spectra, only in the case of weakly nonlinear processes, while experimental reality deals with cascades significantly "contaminated" by effects of a finite size fluid domain, wave breaking, wave cusps, nonlinear dispersion, viscous damping of wave-field components, etc. The very specific dispersion relation for internal waves introduces additional complications. For instance, in rotating fluids, which have a dispersion relation analogous to stratified fluids, the usefulness of the formalism of wave turbulence as a basis for the studies in rotating turbulence has been reported for experiments only recently [21]. The three dimensional structure of wave attractor and transition to wave turbulence in a rotating annular frustum was recently described in [22]. For internal waves, the question is still fully open, from both experimental and numerical points of view.

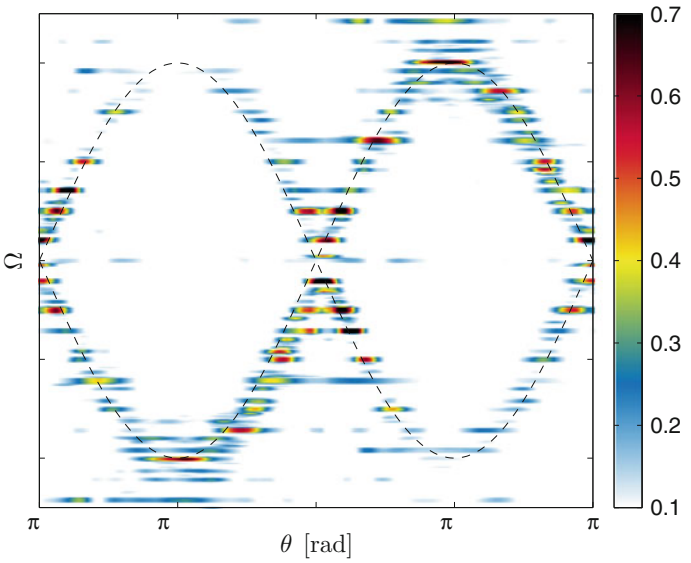

Fig. 9 Energy spectra presented as a function of the non-dimensional frequency Ω and of the slope of the wave beam θ. The dashed lines correspond to the dispersion relation $\Omega = \pm \sin\theta = \pm k_x/\sqrt{k_x^2 + k_z^2}$. Integration across different wavenumbers ranges from 0.22 to 1 rad·cm^{-1}, i.e. wave lengths 28.5–6.3 cm

The presence of wave turbulence-like phenomena is illustrated in Fig. 9 using the energy spectra experimentally obtained for large scales as a diagnostic tool [21]. Horizontal and vertical velocity fields $u(x, z, t)$ and $w(x, z, t)$ are obtained with 2D PIV measurements in the entire trapezoidal domain. A two dimensional Fourier transform for space and a one dimensional Fourier transform for time of these fields leads to $\hat{u}(k_x, k_z, \Omega)$ and $\hat{w}(k_x, k_z, \Omega)$. One can thus define the 2D energy spectrum by

$$E(k_x, k_z, \Omega) = \frac{|\hat{u}(k_x, k_z, \Omega)|^2 + |\hat{w}(k_x, k_z, \Omega)|^2}{2ST}, \tag{8}$$

where S is the area of the PIV measurement and T its duration.

In the dispersion relation for internal waves, $\Omega = \pm \sin\theta$, the wave vector $\mathbf{k}$ and its components do not appear directly but they are linked with the angle θ by $\sin\theta = \pm k_x/\sqrt{k_x^2 + k_z^2}$. To compute the energy spectrum as a function of variable θ, one can interpolate the energy spectrum $E(k_x, k_z, \Omega)$ to get $E(k, \theta, \Omega)$, where k is the norm of the wave vector. Then, one can integrate over the entire range of wave vectors $[k_{min}, k_{max}]$ as follows

$$E(\theta, \Omega) = \int_{k_{min}}^{k_{max}} E(k, \theta, \Omega)\, k \, \mathrm{d}k, \tag{9}$$

or on any range of wave vectors between k_{min} and k_{max}. Note that the accessible range of wave vectors $[k_{\mathrm{min}}, k_{\mathrm{max}}]$ is set by the experimental PIV mesh. The integration in Eq. (9) has been done in Fig. 9 with an integration range which represents 84% of the energy in the entire range $[k_{min}, k_{max}]$. The linear dispersion relation is seen to attract the maxima of the energy spectra. Above results are convincing signatures of a discrete wave turbulence framework for internal waves in this intermediate forcing amplitude regime.

If we repeat the same experiment with a larger amplitude, we have indications that the system is beyond the wave turbulence-like regime and has reached a mixing regime. Indeed, short-scale perturbations in particular clearly escape any relation to linear wave dynamics. This is expected to be due to overturnings, natural precursors to mixing.

Mixing Inferred from Vorticity Distribution

An important issue is whether or not sufficiently energetic internal wave motion can produce an irreversible energy contribution to mixing. Figure 10a presents the comparison between density profiles measured before and after experiments: while no modification of the density (within experimental error) can be observed for the intermediate amplitude forcing that leads to wave turbulence regime described in the previous section, one gets a clear evidence of mixing in case of a larger forcing amplitude.

Further, differences between the regimes corresponding to low and high mixing are clearly seen in statistics of extreme events. This statistics is obtained by the calculation of probability density functions (PDF). Since we are interested in small-scale events destabilizing the stratification, we take the horizontal y-component of vorticity $\xi(x, z, t) = \partial u/\partial z - \partial w/\partial x$ measured in the vertical midplane of the test tank as a relevant quantity and consider the PDF of the dimensionless quantity ξ/N. In Fig. 10b, we present the vorticity PDFs corresponding to different wave regimes in the attractor. In a stable attractor (see dash-dotted curve), extreme events are completely absent and the wave motion is concentrated within the relatively narrow branches of the attractor while the rest of the fluid is quiescent. Accordingly, the PDF has a sharp peak at zero vorticity and is fully localized between well-defined maximum and minimum values of vorticity. For larger forcing amplitudes (dashed and solid curves), the development of TRI increases the probability of extreme events due to summation of primary and secondary wave components.

The occurrence of local overturning events can be viewed as a competition between stratification and vorticity. In a two-dimensional flow, a relevant stability parameter is a version of the Richardson number, which can be introduced as $\mathrm{Ri}_{\xi} = N^2/\xi^2$. For a horizontal stratified shear flow this parameter reduces to the conventional gradient Richardson number $\mathrm{Ri} = N^2/(\mathrm{d}u/\mathrm{d}z)^2$, where $\mathrm{d}u/\mathrm{d}z$ is the velocity shear. Flows with large Ri are generally stable, and the turbulence is suppressed by the stratification. The classic Miles-Howard necessary condition for instability

requires that $\mathrm{Ri} < 1/4$ somewhere in the flow. If this condition is satisfied, the destabilizing effect of shear overcomes the effect of stratification, and some mixing occurs as a result of overturning. The threshold value $|\xi/N| = 2$ is marked on the plot of vorticity PDFs. It can be seen that data corresponding to large forcing amplitudes have "tails" extending into the domains $|\xi/N| > 2$. The area under the tails represents the probability of event of strength $|\xi/N| > 2$. In the larger forcing case (solid curve), this probability is an order of magnitude greater than in intermediate one (dashed curve), in qualitative agreement with the much higher mixing that has been reported.

Conclusion

The paramount importance of a cascade of mechanical energy in the dynamics of the ocean comes from the fact that the ocean is not a classic heat engine: mechanical forcing is needed to drive the meridional heat flux and deep-water renewal. The closure of the meridional circulation critically depends on the cascade of mechanical energy in the abyss and its contribution to mixing.

In the present work, tackling this question with a physicist approach,

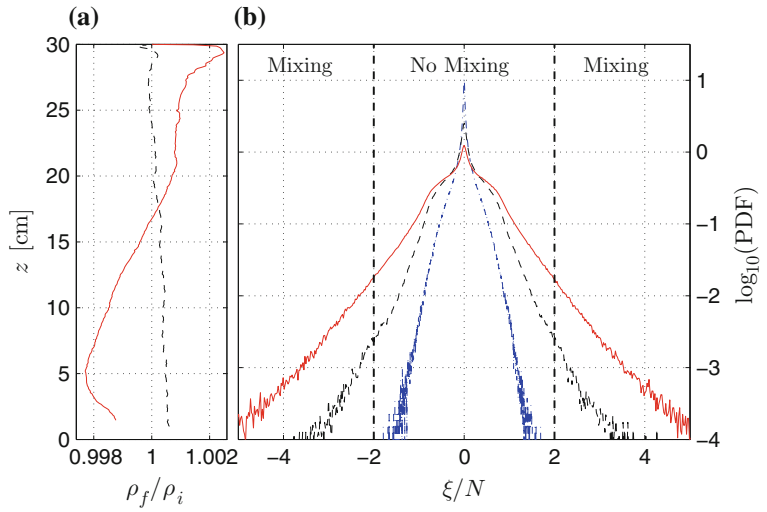

Fig. 10 **a** Ratio between the density profiles measured after and before the experiments for cases with intermediate (dashed) and large (solid) forcing amplitudes. **b** Experimental probability density functions of the vorticity, calculated on the grid from experimental images for low (dotted), intermediate (dashed) and large (solid) forcing amplitudes. Figures 8 and 9 correspond to the intermediate forcing amplitude

- We propose a unique self-consistent experimental (and also numerical) set-up that models a cascade of triadic interactions transferring energy from large-scale monochromatic input to multi-scale internal wave motion.
- We provide explicit evidences of a wave turbulence framework for internal waves, with a clear transition to a cascade of small-scale overturning events.
- We show how beyond the wave turbulence, this original set-up can induce mixing that can be inferred from the calculation of the potential energy or directly by measuring the stratification.

We take advantage of elaborate and recent signal processing tools (Hilbert transforms, time-frequency analysis, bicoherence, ...) to analyze experimental and numerical data. The observed model cascade employs wave attractors, whose significance is realized for stratified and/or rotating fluids (i.e. for a very broad class of celestial bodies) and for magnetized materials, attesting cross-disciplinary importance of the present study for a broad scientific community.

Confinement of the fluid domain and focusing of wave energy at an attractor play an important role in the cascade. However, these conditions are not very restrictive. Under natural conditions internal waves can travel thousands of kilometers which means that quite large bodies of water (for instance, seas) can be considered as confined domains. Also, since attractors can occur in laterally open domains [23], the mechanism of the triadic wave cascade and the bulk mixing described in the present paper is likely to occur in domains with multi-ridge topography as described in [3].

Physical systems supporting wave attractors are strong sources of natural wave turbulence and provide an "internal wave mixing box" that can give useful insights, in the laboratory, on abyssal mixing.

Acknowledgements This work was supported by the LABEX iMUST (ANR-10-LABX-0064) of Université de Lyon, within the program "Investissements d'Avenir" (ANR-11-IDEX-0007) operated by the French National Research Agency (ANR). This work has achieved thanks to the resources of PSMN from ENS de Lyon. E.V.E. gratefully acknowledges his appointment as a Marie Curie incoming fellow at Laboratoire de physique ENS de Lyon. INS is gratefull for support Russian Foundation for Basic Research 15-01-06363 and Russian Science Foundation 14-50-00095. Direct numerical simulations were performed on supercomputer Lomonosov of Moscow State University. We thank L. Maas, G. Pillet and H. Scolan for helpful discussions and D. Le Tourneau and M. Moulin for technical assistance.

References

1. Morozov, E. G. (1995). Semidiurnial internal wave global field. *Deep-Sea Research*, *I*(42), 135–148.
2. Egbert, G. D., & Ray, R. D. (2000). Significant dissipation of tidal energy in the deep ocean inferred from satellite altimeter data. *Nature*, *495*, 775–778.
3. Polzin, K. L., Toole, J. M., Ledwell, J. R., & Schmitt, R. W. (1997). Spatial variability of turbulent mixing in the Abyssal Ocean. *Science*, *276*(5309), 93–96.
4. Nazarenko, S. V. (2011). *Wave turbulence*. Lecture Notes in Physics, Berlin: Springer.
5. Maas, L. R. M., Benielli, D., Sommeria, J., & Lam, F. P. A. (1997). Observations of an internal wave attractor in a confined stably stratified fluid. *Nature*, *388*, 557–561.

6. Brouzet, C., Sibgatullin, I.N., Ermanyuk, E.V., Joubaud, S., & Dauxois, T. (2017). Scale effects in internal wave attractors. *Physical Review Fluids*, *2*, 114803.
7. Scolan, H., Ermanyuk, E. V., & Dauxois, T. (2013). Nonlinear fate of internal waves attractors. *Physical Review Letters*, *110*, 234501.
8. Bourget, B., Scolan, H., Dauxois, T., Le Bars, M., Odier, P., & Joubaud, S. (2014). Finite-size effects in parametric subharmonic instability. *Journal of Fluid Mechanics*, *759*, 739–750.
9. Dauxois, T., Joubaud, S., Odier, P., & Venaille, A. (2018). Instabilities of internal wave beams. *Annual Review of Fluid Mechanics*, *50*, 131–156.
10. Phillips, O. M. (1966). *The dynamics of the upper ocean*. New York: Cambridge University Press.
11. Dauxois, T., & Young, W. R. (1999). Near-critical refection of internal waves. *Journal of Fluid Mechanics*, *390*, 271–295.
12. Maas, L. R. M., & Lam, F. P. A. (1995). Geometric focusing of internal waves. *Journal of Fluid Mechanics*, *300*, 1–41.
13. Berry, M. V. (1981). Regularity and chaos in classical mechanics, illustrated by three deformations of a circular billiard. *European Journal of Physics*, *2*, 91–102.
14. Fischer, P. F. (1997). An overlapping Schwarz method for spectral element solution of the incompressible Navier Stokes equations. *Journal of Computational Physics*, *133*, 84–101.
15. Fischer, P. F, Mullen, J. S. (2001). Filter-based stabilization of spectral element methods. *Comptes rendus de l'Académie des Sciences Paris Series I–Analyse Number*, *332*, 265–270.
16. Brouzet, C., Sibgatullin, I., Scolan, H., Ermanyuk, E. V., & Dauxois, T. (2016). Internal wave attractors examined using laboratory experiments and 3D numerical simulations. *Journal of Fluid Mechanics*, *793*, 109–131.
17. Brouzet, C. (2016). *Internal wave attractors: from geometrical focusing to non-linear energy cascade and mixing*. Ph.D. dissertation, ENS de Lyon. https://tel.archives-ouvertes.fr/tel-01361201/en.
18. Gostiaux, L., Didelle, H., Mercier, S., & Dauxois, T. (2007). A novel internal waves generator. *Experiments in Fluids*, *42*(1), 123–130.
19. Mercier, M. J., Martinand, D., Mathur, M., Gostiaux, L., Peacock, T., & Dauxois, T. (2010). New wave generation. *Journal of Fluid Mechanics*, *657*, 308–334.
20. Brouzet, C., Ermanyuk, E. V., Joubaud, S., Sibgatullin, I. N., & Dauxois, T. (2016). Energy cascade in internal wave attractors. *Europhysics Letters*, *113*, 44001.
21. Yarom, E., & Sharon, E. (2014). Experimental observation of steady inertial wave turbulence in deep rotating flows. *Nature Physics*, *10*, 510–514.
22. Sibgatullin, E., Ermanyuk, L., Maas, X., Xu & Dauxois, T. (2017). *Directnumerical simulation of three-dimensional inertial wave attractors*. Ivannikov ISPRAS open conference 2017 (ISPRAS) (pp. 137-143). Moscow, Russia.
23. Echeverri, P., Yokossi, T., Balmforth, N. J., & Peacock, T. (2011). Tidally generated internal-wave attractors between double ridges. *Journal of Fluid Mechanics*, *669*, 354–374.